Additive Manufacturing 71 (2023) 103587

Contents lists available at ScienceDirect

Additive Manufacturing

journal homepage: www.elsevier.com/locate/addma

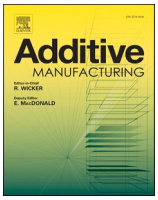

Thermoelectric magnetohydrodynamic control of melt pool flow during laser directed energy deposition additive manufacturing

Xianqiang Fan [a,b,*], Tristan G. Fleming [c], David T. Rees [a,b], Yuze Huang [f], Sebastian Marussi [a,b], Chu Lun Alex Leung [a,b], Robert C. Atwood [e], Andrew Kao [d,**], Peter D. Lee [a,b,*]

[a] UCL Mechanical Engineering, University College London, WC1E 7JE, UK
[b] Research Complex at Harwell, Harwell Campus, Didcot OX11 0FA, UK
[c] Department of Physics, Engineering Physics & Astronomy, Queen's University, K7L 3N6, Canada
[d] Centre for Numerical Modelling and Process Analysis, University of Greenwich, London SE109LS, UK
[e] Diamond Light Source Ltd, Harwell Campus, Didcot OX11 0DE, UK
[f] Centre for Manufacturing and Materials, Coventry University, Coventry CV1 5FB, UK

ARTICLE INFO

Keywords:
Additive manufacturing
Melt flow control
Thermoelectric magnetohydrodynamic
Magnetic fields
Tungsten tracer

ABSTRACT

Melt flow is critical to build quality during additive manufacturing (AM). When an external magnetic field is applied, it causes forces that alter the flow through the thermoelectric magnetohydrodynamic (TEMHD) effect, potentially altering the final microstructure. However, the extent of TEMHD forces and their underlying mechanisms, remain unclear. We trace the flow of tungsten particles using in situ high-speed synchrotron X-ray radiography and *ex situ* tomography to reveal the structure of TEMHD-induced flow during directed energy deposition AM (DED-AM). When no magnetic field is imposed, Marangoni convection dominates the flow, leading to a relatively even particle distribution. With a magnetic field parallel to the scan direction, TEMHD flow is induced, circulating in the cross-sectional plane, causing particle segregation to the bottom and side of the pool. Further, a downward magnetic field causes horizontal circulation, segregating particles to the other side. Our results demonstrate that TEMHD can disrupt melt pool flow during DED-AM.

1. Introduction

Laser directed energy deposition (DED) is a type of additive manufacturing, during which powders are continuously deposited from the nozzle into a laser melt pool [1,2]. Compared to laser powder bed fusion (LPBF), DED has the advantages of high manufacturing speed and producing parts with site-specific composition, although the complexity of design shapes is more limited. Key areas where the application of DED is being considered are component repair and surface coating [1–3]. However, many challenges still remain for DED, including limited geometric precision [4], and undesirable microstructural features including porosity [5], cracks [6], and large epitaxial columnar grain growth [7]. Although process optimisation may mitigate the development of some undesired microstructures, it also results in a very narrow process window. By introducing a magnetic field to the AM process, we can potentially expand the process window. For instance, when printing a complex geometry part, one combination of process parameters may be optimal for some regions but may fail in others. By applying a magnetic field, we hope to have a higher tolerance for selecting suitable process parameters. These microstructural features are largely controlled by the melt pool flow. In general, the melt pool flow affects the solidification microstructure in several ways. Firstly, the microstructure is primarily controlled by the local thermal gradient and solidification rate, which can be strongly manipulated by the melt flow. Secondly, the flow can transport solute to certain regions, which can increase or decrease the local constitutional undercooling, potentially resulting in a change in the solidification mode. Thirdly, the melt pool flow can significantly affect the melt pool geometry which is a consequence of heat and mass transport. The change in the melt pool geometry can affect the grain growth orientation, leading to distinctive texture and grain morphology. Hence, melt pool flow is central to the melt pool dynamics [8–10], solidification [11] and microstructural feature formation [12,13]. However, an effective way of controlling melt pool flow is still lacking due to the melt pool's small-scale (ca. 1 mm in length in DED [14–16]) and

* Corresponding authors at: UCL Mechanical Engineering, University College London, WC1E 7JE, UK.
** Corresponding author.
E-mail addresses: xianqiang.fan.19@ucl.ac.uk (X. Fan), A.Kao@greenwich.ac.uk (A. Kao), peter.lee@ucl.ac.uk (P.D. Lee).

https://doi.org/10.1016/j.addma.2023.103587
Received 12 January 2023; Received in revised form 7 April 2023; Accepted 1 May 2023
Available online 3 May 2023

elevated temperature. In AM or laser welding, in some material systems, surfactants such as sulphur and oxygen can be added to modify the Marangoni flow. This is particularly applicable in high sulphur stainless steel and oxidised aluminium and titanium powder [8,17–23]. However, these surfactants alter the material composition and may have a detrimental effect on properties [21], and leading to failure during operation. Varying process parameters can also modify the melt flow behaviour, but it will also affect track size and other factors, potentially leading to undesirable results. For example, under certain conditions, increasing energy density can result in the formation of keyhole porosity [24]. New techniques are being sought to control melt flow without adding surfactants or varying process parameters.

The application of external fields, including magnetic fields as a non-contact and contamination-free technique, has great potential for controlling the melt flow in AM. Previous work has largely used electric magnetic damping (EMD) or the Hartman effect to reduce melt pool flow rates [25,26]. However, EMD is not the only magnetic field effect, as the Seebeck effect has also been observed during the related welding process. For instance, Paulini et al. [27] observed the beam deflection during the electron beam welding of dissimilar materials. In a separate study, Kern et al. [28] reported that the surface roughness of an Al weld bead can either be more smooth or rough, depending on the orientation of the applied magnetic field. In both cases, the observed effects were attributed to the Seebeck effect. The Seebeck effect induces thermoelectric currents (TECs) that are a function of the variations of the Seebeck coefficient (due to phase, temperature and compositional variations) and thermal gradient in the laser melt pool [29]. TECs interact with an external magnetic field, generating a Lorentz force that drives a new flow, known as thermoelectric magnetohydrodynamic (TEMHD) flow. TEMHD flow has been proven useful to control solute segregation [30–33] and refine dendrite arm spacing [34,35] in traditional casting and realising self-stirring for liquid lithium [36,37].

Computational modelling has been conducted to predict TECs in both welding [29,38–40] and LPBF [41,42]. The strongest TECs are predicted near the solid/liquid boundary due to sharp variations in the Seebeck coefficient. In DED, TECs are expected to be concentrated at the bottom and back of the melt pool where the solid/liquid solidification interface causes large compositional and thermal gradients, and the Marangoni flow is weakest. Therefore, the TEMHD effect may be quite significant in these areas when a magnetic field is applied. However, to date, no experimental or modelling work for investigating the TEMHD effect in DED has been reported.

Melt flow visualisation techniques are the key to understanding the mechanism of TEMHD control. Significant efforts have been placed to investigate the flow behaviour under TEMHD in welding and LPBF, but are largely restricted to computational modelling [38–42]. Recently, in situ synchrotron X-ray imaging has been applied in AM to directly observe the highly transient phenomena including keyhole dynamics [24,43,44], pore behaviour [12], and powder-melt interaction [45]. Although melt pool flow visualisation using tungsten tracers has been reported in previous work [8–10,46], it remains unclear how the flow will change when applying a magnetic field. In this study, the authors developed a method/tool that combines the flow tracer technique, x-ray imagining, and a series of customised image processing techniques. This method allowed for a detailed investigation of melt pool flow information during the DED process when a magnetic field is present. Here, we applied a magnetic field (B) at multiple orientations, B//V (parallel to the scan velocity (V)) and B downward (parallel to the build direction), during DED of a high γ' nickel superalloy powder blended with tungsten particles. We used a combination of in situ X-ray radiography and *ex situ* tomography to observe TEMHD flow in the melt pool. A series of experiments were designed and performed to reveal the structure of TEMHD flow during DED.

2. Materials and methods

2.1. Materials

The samples used were high γ' nickel superalloy substrates and powders of the same composition (provided by Rolls-Royce plc.), as shown in Supplementary Table 1. For all the experiments, we used the same blended powder consisting of 4 wt% W particles mixed with the γ' nickel superalloy power. Fig. 1 shows SEM images of the γ' nickel superalloy and tungsten powders and their size distribution. According to our calculation (see supplementary), the addition of 4 wt% tungsten can provide 520 tungsten tracers within a melt pool. These tracers account for only 1.9 vol% of the total melt pool volume, suggesting that their presence is unlikely to have a significant impact on the flow. The substrates were cut into pieces of 70 × 20 × 1.5 mm by electro-discharge machining. The γ' nickel superalloy powders were produced by gas atomisation with a spherical morphology. To prepare the blended power for the experiments, we followed a specific procedure. We started by placing the two types of powders in a 250 ml container. Then we repeatedly inverted the container for 15 mins to ensure that the powders were thoroughly mixed. Finally, we loaded the blended power into the powder feeder for use in the experiments.

2.2. DED rig

We built a custom DED rig, or Blown Powder AM Process Replicator, generation II (BAMPR-II), by integrating a Ytterbium-doped fibre laser (SPI Lasers Ltd, UK), a powder feeder (Oerlikon Metco TWIN-10-C), a three-axis motion stage (Aerotech, US), an Ar-filled environment chamber (Saffron, Scientific Equipment Ltd) and a DED nozzle (provided by Rolls-Royce plc.). The laser wavelength was 1070 nm and the maximum laser power was 200 W. The laser was operating in continuous-wave mode, providing a Gaussian beam profile and a laser spot size of 360 μm ($1/e^2$) at the focus. DED experiments were conducted using a combination of three different laser powers (100 W, 160 W and 200 W) and three different magnet configurations (no B, B//V and B downward, as shown in Fig. 2). The laser is stationary with the sample stage moving at a constant speed (traverse speed) of 1 mm/s to build 8 mm long tracks for all trials. In the experiments without a magnetic field, the substrate was mounted on the sample holder without magnets. To provide the magnetic field, we used two cubic NdFeB permanent magnets, each measuring 40 × 40 × 20 mm. These magnets were positioned 2 mm below the deposition location, with a 5 mm gap between them. An aluminium holder was used to assemble the magnets. During the process, the laser remained stationary, while the substrate and magnet holder were connected and moved together, ensuring a steady magnetic field in the melt pool. In the B//V case, the magnets were placed in a holder with the south pole towards the scan direction, providing a magnetic field parallel to the scan direction (see Fig. 2c). To switch the magnetic field orientation, the magnets were turned by 90 degrees, which provided a downward magnetic field on the substrate top surface (see Fig. 2d). All the tracks were built three layers in the middle of the substrates, where the intensity of the magnetic field was 0.18–0.2 T, to ensure an even magnetic field and consistent conditions. Note that the magnetic field intensity at the deposition area was measured three times using a Gauss meter.

2.3. In situ synchrotron X-ray imaging

In situ synchrotron X-ray imaging experiments were performed at beamline I12 of Diamond Light Source at Rutherford Appleton Laboratory, UK [47]. A monochromatic beam with an energy of 70 keV was used for all the experiments. X-rays transmitted through the sample while laser melting were converted to visible light using a scintillator and the images were acquired by a high-speed camera MIRO 310 M (Vision Research Inc.) at a frame rate of 5 kHz, exposure time of 198 μs,

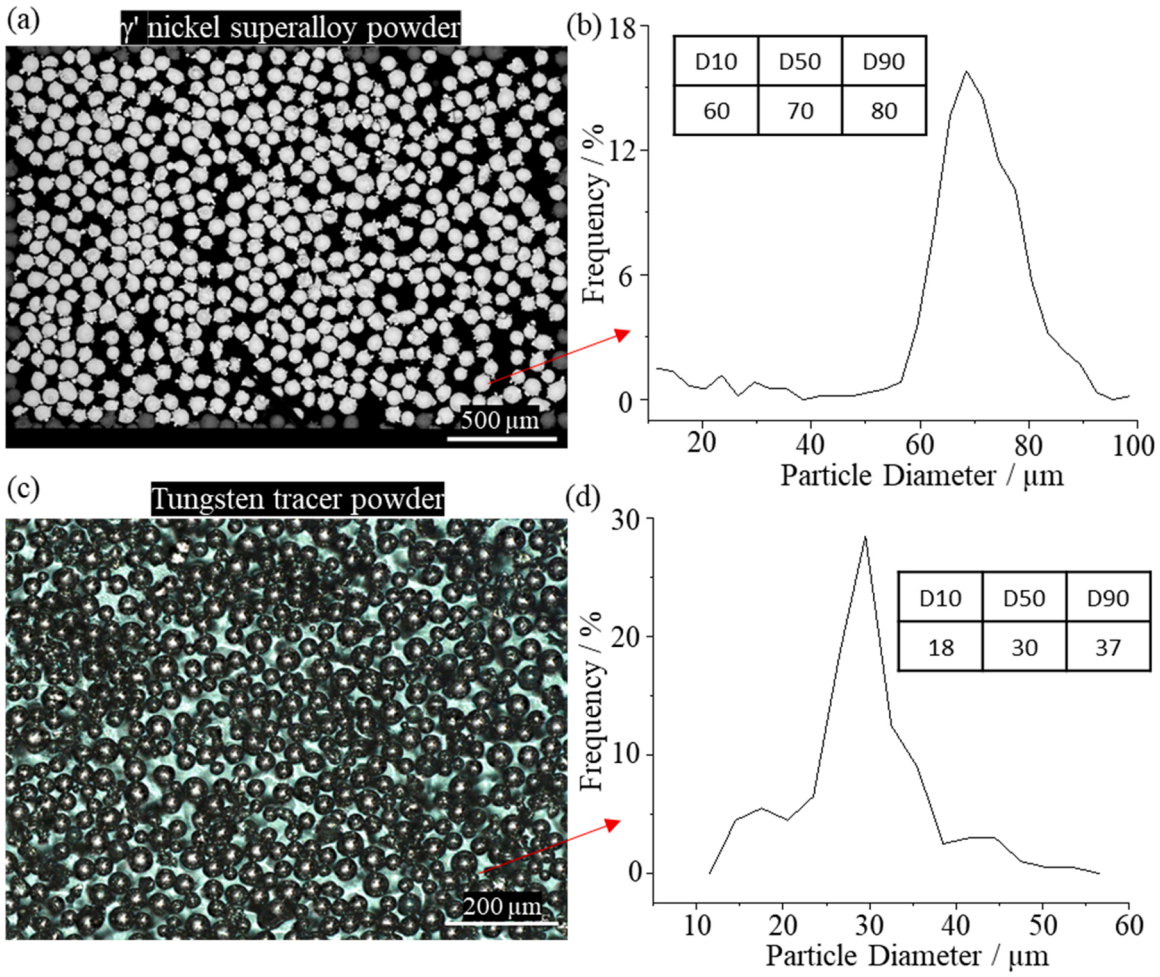

Fig. 1. SEM images of the as-received powders and their size distribution. (a) γ' nickel superalloy powder. (b) Powder size distribution of the γ' nickel superalloy powder. (c) Tungsten tracer powder. (d) Powder size distribution of the tungsten tracer powder.

and a spatial resolution of 6.67 μm/pixel. Prior to laser melting, both flat and dark images were collected for flat field correction to remove the background artefacts, as described in our previous work [13,48].

2.4. Ex situ X-ray computed tomography

The as-built tracks were examined by a laboratory-based X-ray computed tomography system (Nikon XTek2DCT, Nikon, Japan) with an accelerating voltage of 220 kV, beam current of 31 μA and spatial resolution of 3.36 μm. The collected radiographs were reconstructed into a 16-bit image stack with a built-in reconstruction algorithm. Avizo 3D 2021.01 (Thermo Fisher Scientific, USA) was then used for W particle segmentation, quantitative analysis and 3D visualization.

2.5. Data analysis

2.5.1. Image processing of raw data

All the acquired raw radiographs were firstly processed using Matlab R2021a to remove the noise and background. Firstly flat-field correction was applied using the averaged flat and dark images collected during the experiments, after that, a denoise algorithm VBM4D [49] was used to mitigate the noise, followed by a further background subtraction process using a customised approach. Then the processed data with high contrast and low noise can be further analysed for extracting useful information, such as particle trajectories and velocities.

2.5.2. Tungsten particle tracking

Prior to tracking, the radiographs were integrated through the duration of the experiment to enable the visualisation of the W particle trajectories. The time-integrated radiographs were obtained by overlaying the particles in successive frames onto one plane. Then the particles are tracked using TrackMate [50] in ImageJ. A particle tracking example is shown in Movie S1. It is worth noting that small particles are likely to reliably trace flow, as the motion of large particles is potentially influenced by the TECs inside the particles when applying a magnetic field. The critical particle size that separates the as-classified small and large particles were found to be 55–65 μm (See Supplementary Fig. 1). Therefore, here only small particles with a size less than 65 μm were considered for understating the melt pool flow behaviour.

3. Results

3.1. DED melt pool flow

The flow conditions with no applied magnetic field were studied first, captured using in situ synchrotron radiography while depositing single DED tracks using three different laser powers. The radiographs of the melt pool were then integrated over the duration of each deposit to visualise the flow of W particles (Fig. 3a-b). Fig. 3b-d highlight typical particle trajectories as the power is increased from 100 to 200 W. In all cases the particles (and hence flow) move slowly up the centre of the pool (50–120 mm/s), reaching the surface. They then turn outwards, accelerating outwards along the surface driven by Marangoni

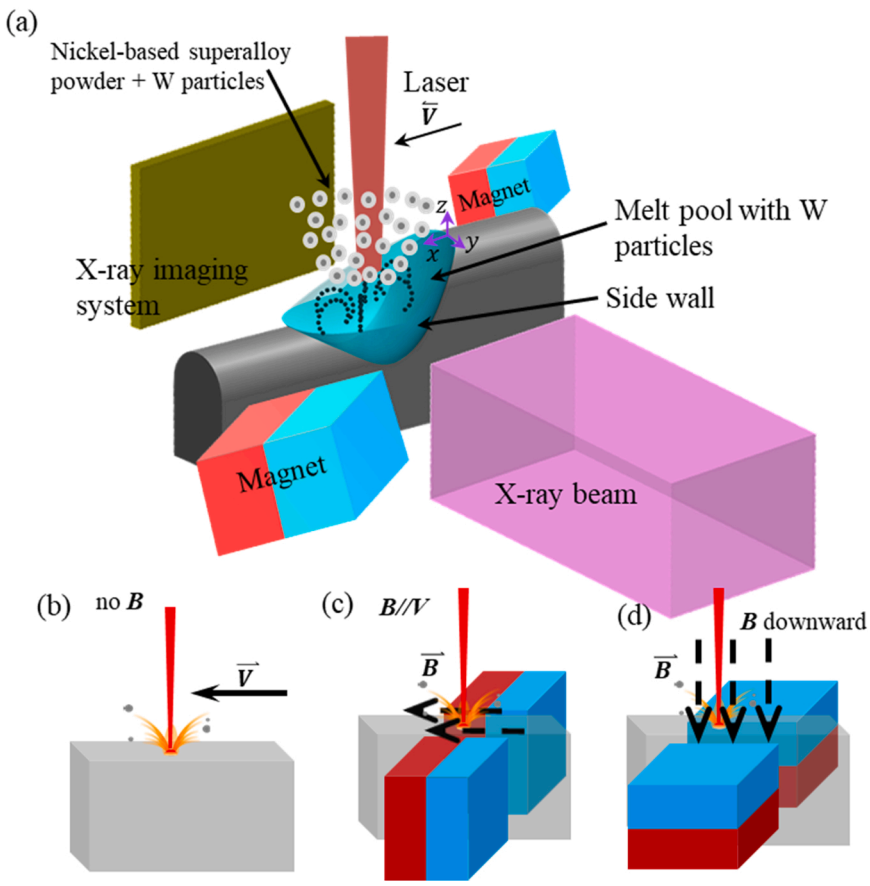

Fig. 2. (a) Experiment setup of in situ synchrotron X-ray imaging of magnetic-field-assisted DED; (b) Setup of the no B case; (c) Setup of the B//V case; (d) Setup of the B downward case. Nickel-based superalloy powders were blended with W particles to be deposited on the thin substrate (1.5 mm thickness). The laser was kept stationary with a substrate moving at 1 mm/s traverse speed for unidirectional scan for all the builds with a stationary melt pool generated in the field of view. X-rays pass through the melt pool to image the melt pool at the framerate of 5 kHz, the resolution is 6.67 μm per pixel. The applied laser powers are 100, 160 and 200 W. Three layers for all the tracks. Two permanent magnets were mounted around the substrate to provide a uniform magnetic field (0.18–0.2 T) in the melt pool position.

convection. The peak particle velocity occurs at the melt pool surface in all cases, increasing with increasing laser power (peak velocity of ca. 220 mm/s, 280 mm/s, and 310 mm/s at 100, 160, and 200 W, respectively, see Fig. 3e). The particles then slow (velocity of 20–50 mm/s) as the flow reaches the outer solid/liquid boundary, turning downwards, forming a recirculating flow.

3.2. DED melt pool flow under external magnetic field

Here, we selected an exemplary case (laser power $P = 100$ W, laser scan speed $V = 1$ mm/s) to compare the melt flow behaviour without and with magnetic fields. Without an external magnetic field, the particle velocity at the surface exceeds 200 mm/s (due to Marangoni flow, see Fig. 3e), as described above, the particles turn downwards as they near the edge of the pool surface, turning downwards into the pool. The particles decelerate as they approach the bottom of the melt pool, reaching a minimum speed of 20–50 mm/s before turning direction and recirculating back up in the middle of the pool towards the surface (see Fig. 4a, b and Movie S2). Of those particles in the back half of the pool, some are entrained in the solidification front, and are relatively evenly distributed in the new solidified track, as shown in the pink box in Fig. 4a.

When a magnetic field is applied, the peak particle velocity at the surface of the pool is similar to that without a magnetic field, reaching ca. 200 mm/s. However, as the particles move towards the bottom of the pool, a TEMHD flow becomes dominant. In the B//V case, particles velocities were found to be reduced to 1–2 mm/s as they approached the bottom, with the particle trajectories along the front of the pool all heading downwards, even in the middle of the pool where previous the flow was strongly upwards. Almost all are captured at the pool bottom (Fig. 4c, d and Movie S3), forming a layer separating the new track from the prior ones. This observation can be attributed to the introduction of a Lorentz force. Near the bottom of the melt pool, the upward Lorentz force counteracts the downward Marangoni flow, leading to a stagnant flow in this region. As a result, particles tend to sink at a slow speed. The origin of this Lorentz force will be introduced in the discussion section.

For the case where a downward magnetic field was applied, the particles even in the rear of the pool are turned and driven almost horizontally into the rear solid/liquid interface where they are entrained. The particles are entrained at a range of heights in the pool, although the majority are in the lower half (see Fig. 4e, f and Movie S4). These observations strongly support the hypothesis that the flow in the melt pool is altered when applying a magnetic field, and the effect depends on the magnetic field orientations.

Radiography is restricted to a longitudinal plane projection and does not provide information about flow in the cross-sectional plane (in/out of the page). Therefore, we used X-ray computed tomography to observe the effects of applied magnetic fields on the final particle locations inside the built samples. The reconstructed 3D as-built tracks with W particles embedded are shown in Supplementary Fig. 2. By overlaying particles onto one cross-sectional plane, the overall distribution of the W particles in the entire track can be visualised (see Supplementary Fig. 3).

Fig. 5a shows that the particles are evenly distributed in the solidified tracks in the horizontal projection plane when no magnetic field is applied, matching the even longitudinal distribution in all three laser powers (Fig. 6a-c). In general, particles tend to segregate equally to the two sides of the melt pool due to Marangoni flow. However, the extent of such segregation depends on various factors, including material properties, process parameters, and particle number density. Based on the material, and the process parameters used in this study, along with the small number of tracer particles, we observed a relatively even distribution of particles. However, it's worth noting that a valley is distinguishable in Fig. 7 g, indicating very weak particle segregation in the no B case. We believe for increased particle number densities, the particle

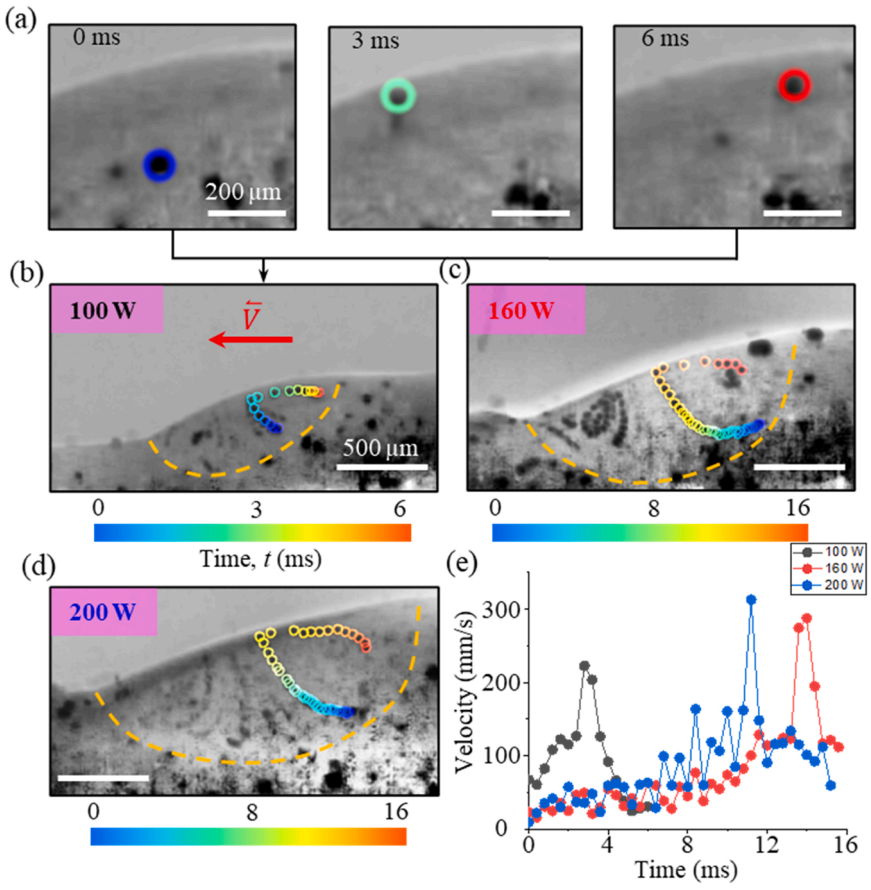

Fig. 3. Flow behaviour without magnetic field. (a) Three successive radiographs showing a tungsten (W) particle's trajectory, coloured by time. (b-d) Time-integrated radiographs showing W particles trajectories under no B case at various laser powers: (b) 100 W; (c) 160 W; (d) 200 W. (e) W particle velocity versus time with three laser powers, corresponding to the coloured trajectories in (b-d). The sample traverse speed is 1 mm/s for all the cases.

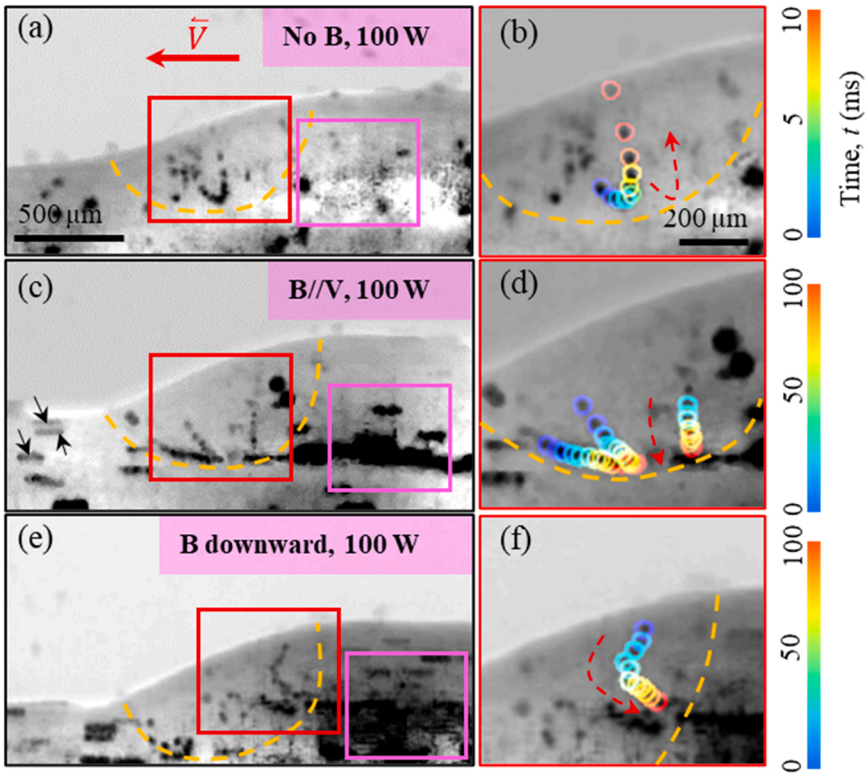

Fig. 4. Comparison of W particle trajectories without and with the magnetic field (B). (a, b) no B case; (c, d) B//V case (V denotes the laser scan velocity); (e, f) B downward case; (b, d, f) is the zoom-in of the red box areas in (a, c, e). In the solid phase, tungsten (W) particles form straight black lines parallel to each other (see black arrows in c as examples) as a result of the time integration of radiographs. Pink boxes highlight the particle distribution in the solidified tracks: evenly distributed in (a) with no magnetic field; segregated to the very bottom of the pool in (c) for the B//V case; and segregated to the bottom half of the pool for (e), the B downward case.

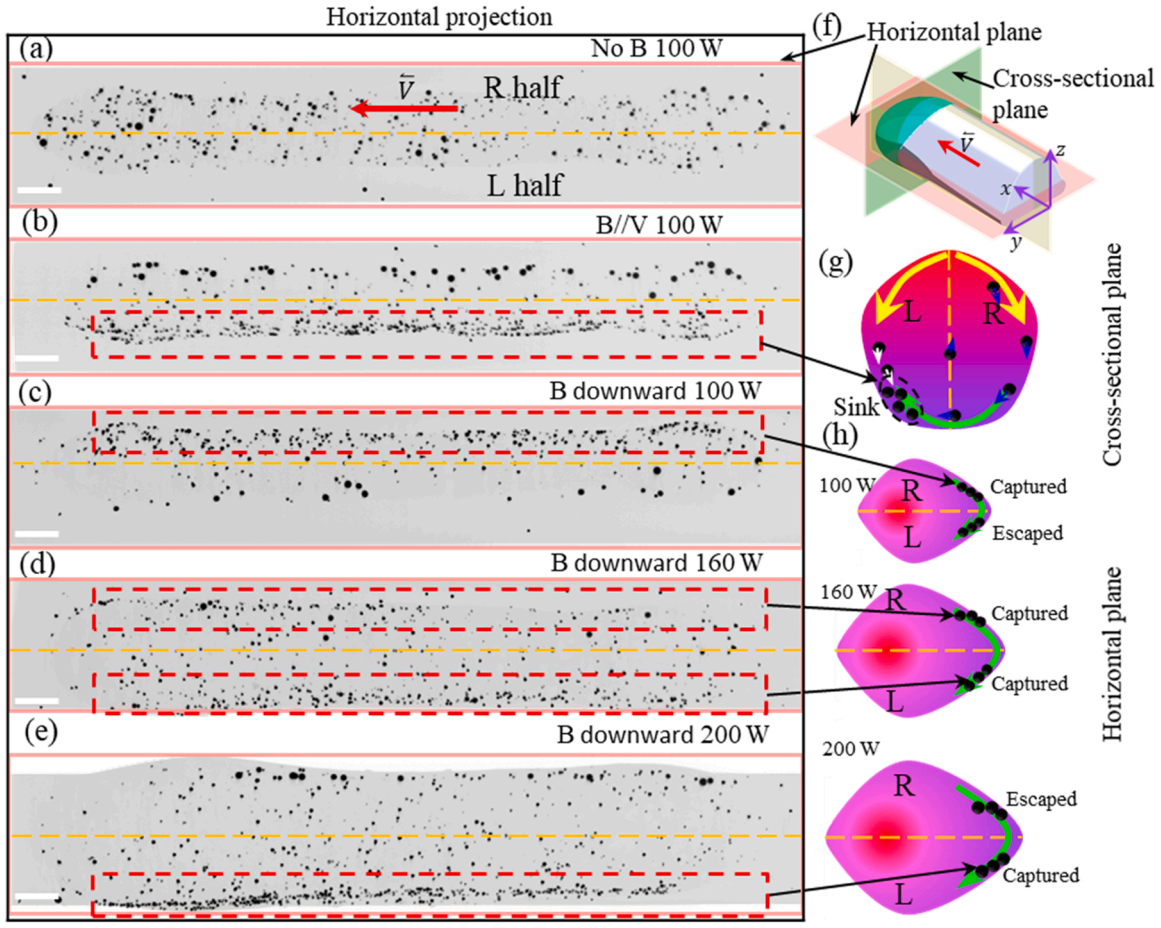

Fig. 5. Tungsten particles segregation under various conditions. (a) No B, 100 W; (b) B//V, 100 W; (c) B downward, 100 W; (d) B downward, 160 W; (e) B downward, 200 W. (f) The schematic shows the three orthogonal planes; (g) TEMHD flow circulating in the cross-sectional plane in the B//V case; and (h) TEMHD flow circulating in the horizontal plane under the B downward case. The particles are overlaid onto one tomograph in a horizontal projection plane. (Red arrow = scan direction. Green arrows = TEMHD flow. Yellow arrows = Marangoni flow. Scale bar = 500 μm.).

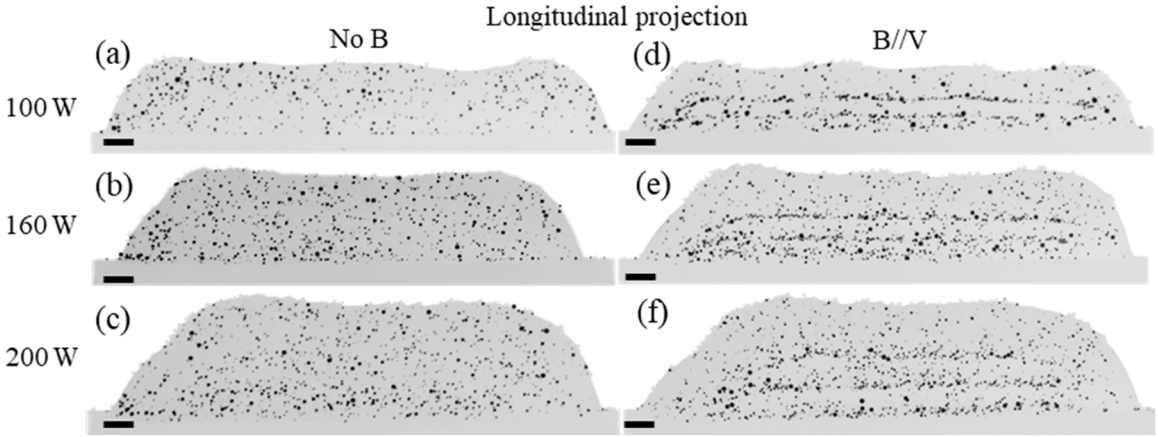

Fig. 6. Distribution of W particles in the solidified tracks in the longitudinal projection planes under conditions: (a) no B, 100 W; (b) no B, 160 W; (c) no B, 200 W; (d) B//V, 100 W (e) B//V, 160 W and (f) B//V, 200 W. All built in three layers. The scale bars are 500 μm.

segregation into two sides will become more obvious. However, we added a small number of particles to minimise their influence on the flow whilst observing the effect of the magnetic field on flow. Applying a magnetic field orientated in the laser scan direction (the B//V case) disrupts this even distribution. In addition to segregating the particles to the bottom of the pool (as per Fig. 4c and Fig. 6d-f), the external magnetic field also drove them to one side of the track (see Fig. 5b). To make the description clear, the melt pool was divided into two halves, i.e., Left (L) and Right (R) halves corresponding to looking along the scan direction (see Fig. 5a, f). In the B//V case, the location of particles segregation is the L half of track for all three laser powers (see Fig. 5b and Supplementary Fig. 4c, d). Prior authors [26,51–54] have suggested the electromagnetic dampening effect (EMD) is the cause, but this force only reduces the magnitude, not the direction. Therefore, it will not alter

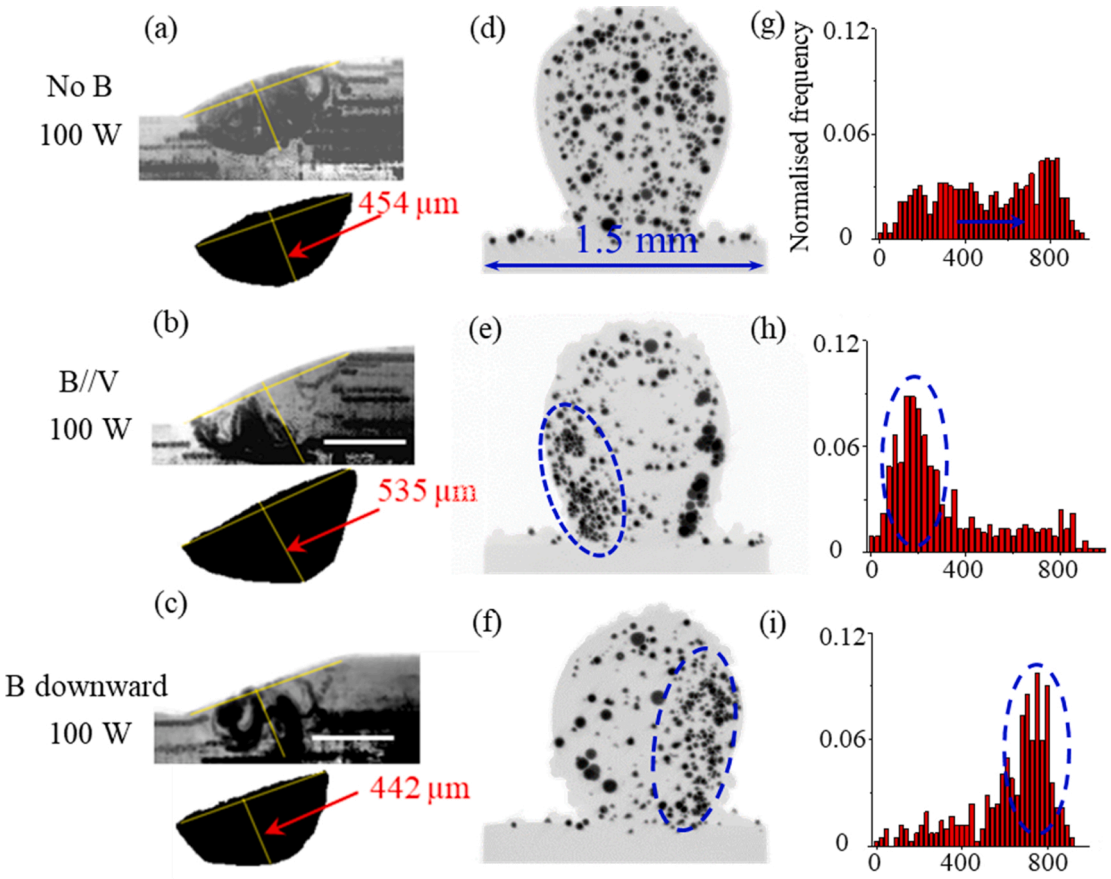

Fig. 7. Comparison of the melt pool depth under the conditions of (a) no B, 100 W; (b) B//V, 100 W; (c) B downward, 100 W. The melt pools are filled with W particle trajectories to show the liquid area, i.e., the melt pool area. Distribution of W particles in the solidified tracks in the cross-sectional projection plane under conditions: (d) no B, 100 W; (e) B//V, 100 W; (f) B downward, 100 W, and (g-i) show the corresponding normalized frequency of W particles along substrate width. All built in three layers. The widths of all the substrates are 1.5 mm. The scale bars are 500 μm.

the segregation pattern and cannot explain our experimental results. Our hypothesis is that a TEMHD flow is introduced by the magnetic field as a result of the Seebeck effect that induces Thermoelectric currents (TECs), causing asymmetric particle segregation. In the B//V case, the newly introduced TEMHD flow in the left half of the melt pool is in the opposite direction of the Marangoni flow, causing stagnation of flow. As a result, particles settle in this region due to their heavier weight compared to the melt. This process is highlighted in the schematic shown in Fig. 5 g. The TEMHD flow in the right half enhances the transportation of hot liquid down to the bottom, modifying the melt pool shape. As a result, a deeper melt pool (ca. 535 μm in depth) was produced in the B//V case compared to no magnetic field (ca. 454 μm) and B downward cases (ca. 442 μm) (see Fig. 7a-c).

For the B downward case, a TEMHD flow is produced in the horizontal plane, driving particles across the solidification front (see Fig. 5 h). In this case, the final location where the particles segregate to is strongly dependent on the melt pool size, which is controlled by the laser power. For a laser power of 100 W, the melt pool is small (ca. 1 mm in length), most particles segregate to the R half of the track (Fig. 5c). Whereas with 200 W laser power, the melt pool length almost doubles to ca. 2 mm, and more particles remain in the L half (Fig. 5e). With an intermediate laser power (160 W), particles are equally segregate to both halves of the track (see Fig. 5d). This observation can be understood through the balance between Marangoni and TEMHD flows. In the right half, the Marangoni flow has a component in the negative $\hat{y}$ direction, whereas in the left half, it is in the positive $\hat{y}$ direction. The TEMHD-induced flow circulates from right to left near the melt pool boundary (Fig. 5 h), which means that in both the right and left half of the melt pool, TEMHD flow has a component in the positive $\hat{y}$ direction. Increasing the laser power mainly increases the thermal gradient within the melt pool. Although both Marangoni stress and TE Lorentz force increase with the thermal gradient, the TE Lorentz force increases faster than Marangoni stress in the region near the melt pool boundary. At a laser power of 100 W, the Marangoni flow and TEMHD flow are of similar intensity in the $\hat{y}$ direction, leading to flow stagnation in the right half. In the left half, both the Marangoni and TEMHD flows in the $\hat{y}$ direction are positive, resulting in enhanced flow in this region. As a result, more particles can be captured by the solid/liquid interface in the right half. However, particles can escape more easily from the left half. When the laser power is increased to 200 W, in the right half near the boundary region, TEMHD flow overtakes Marangoni flow in the $\hat{y}$ direction, leading to increased flow intensity in the positive $\hat{y}$ direction and more particles escaping from this region. In contrast, in the left half, although both Marangoni and TEMHD flows intensify in the positive $\hat{y}$ direction, TEMHD flow transports more particles to the left half, increasing the particle concentration in the left half hence the chance of being captured by the solidification front. Thereby, more particles are segregated to the left half. When the applied laser power is 160 W, the contribution from flow stagnation and TEMHD transporting particles are balanced, leading to a relatively equal distribution of particles in the two halves of the melt pool.

Fig. 8 shows the comparison of the grain structure of the as-printed tracks on the cross-sectional plane for the three conditions. The results show that applying a magnetic field can alter the central grain structure on the cross-section. The average central grain size in the no B case is 87 μm, and it is reduced to 68 μm in the B//V case and 75 μm in the B

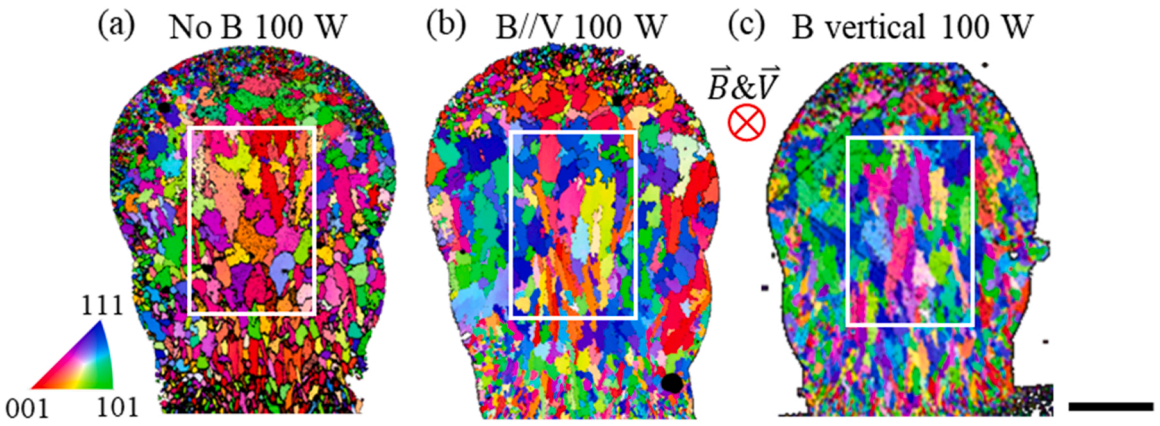

Fig. 8. Comparison of the grain structure under the conditions: (a) no B, 100 W; (b) B//V, 100 W; (c) B vertical, 100 W. The white boxes indicate the central grain areas. The scale bar is 250 μm.

downward case. In addition, in the B//V case, there are thin and elongated grains appearing at the bottom of the melt pool, while in the B downward case, the thin and elongated grains are spread more widely from the bottom to near the surface. This observation can be attributed to the influence of the TEMHD flow. A previous study has demonstrated that increasing flow speed leads to an increase in the size of constitutional undercooling zone, as fast flow draws more solute from the mushy zone to the dendrite tip [11]. The increase in the undercooling zone promotes the nucleation rate and favours the transition from nuclei to grains. In the B//V case, the newly introduced TEMHD flow circulates on the cross-sectional plane at a location near the bottom of the melt pool. This flow increases the size of undercooling zone at the bottom hence an increase in the nucleation rate. In the horizontal dimension, grain growth is restricted by the neighbouring grains, as the increased number of new grains causes less space for each grain to grow in this dimension. In the vertical direction, the grain has more space to grow, resulting in the formation of thin and elongated grains at the bottom (Fig. 8b). For the B downward case, the magnetic field interacts with the TECs located at the wide height range of the rear of the melt pool. The resulting TEMHD flow circulates on the horizontal plane, impacting the rear of the melt pool. More grains form in front of the rear melt pool boundary in a wide height range, which leads to the appearance of thin elongated grains in a wide range of height on the central cross-section plane (Fig. 8c).

To summarise, without a magnetic field the particles are relatively evenly distributed for all conditions. However, for both cases of an applied magnetic field, the particles are segregated, with the extent of segregation depending on laser power for the B downward case. For the B//V case the particles sink to the very bottom of the pool and are entrained there. While for the B downward case, the particles sink slightly to the lower half of the pool. Further, based on our observations, we have found that flow near the melt pool boundary is most affected by the TEMHD effect. Specifically, the rear and bottom boundaries where solidification occurs experience significant flow alternation when applying a magnetic field – a location likely to affect microstructural formation. Moreover, the flow in this area determines how particles (and probably pores) are entrained by the solid. Hence this impacts on the particle segregation pattern in the build, which indicates the regional flow pattern. However, flow at the melt pool surface is still Marangoni stress controlled.

4. Discussion

Thermal electric currents (TECs) arise as a result of the Seebeck effect when there is a gradient in the Seebeck coefficient and temperature. TECs are generated by the term $\sigma S\nabla T$ (J_E) in Ohm's law for current density $J = \sigma(E + u \times B + S\nabla T)$, where E is the electric field, u is the flow velocity, B is the magnetic field flux density, σ is electric conductivity, S is the gradient in Seebeck coefficient or Seebeck powder and ∇T is the thermal gradient. This is used in thermocouples where two dissimilar materials and temperature differences are required to generate the thermoelectric field. In the AM melt pool, the presence of liquid and solid phases, as well as a temperature/composition gradient satisfies all the requirements for generating TECs. TECs are expected to circulate from the hot melt front to the cold solidification front in the solid phase, and the opposite-direction currents form in the liquid phase to preserve charge conservation, as shown in Fig. 9a. Large TECs are expected in the melt pool due to the large thermal gradient. For example, Kern *et al.* [28] measured 8–14 A currents density during laser welding of aluminium alloy. Simulation studies pointed out that TECs are concentrated to the vicinity of the solid/liquid boundary due to the sharp variation of the Seebeck coefficient across the solid/liquid boundary [38–40].

In these DED experiments the two side walls of the melt pool are in contact with non-conducting gas (see Fig. 2a), which would restrict electric current circulations out of the side of the melt pool ($\hat{y}$ direction) i.e., electric currents do not circulate between the liquid and gas. Therefore, the primary TECs are circulating in the longitudinal plane (xz plane), and symmetrically distributed in the cross-sectional (see Fig. 9b) and horizontal planes (see Fig. 9c) without the $\hat{y}$ component of the current, and TECs are expected to be concentrated along the base and back of the melt pool as the solid/liquid boundary locates in these areas. With an applied magnetic field orientated in $+\hat{x}$ (i.e., B//V case), a TE Lorentz force is generated in the form of $F_{lorentz} = J_E \times B$, and induces a new flow that circulates in the cross-sectional plane (i.e., yz plane) close to the base of the melt pool, as shown in Fig. 9d. For the case of downward magnetic field, a TE Lorentz force is created in the horizontal plane (i.e., xy plane) and drives a recirculating flow in this plane near the back of the melt pool, as shown in Fig. 9e. Fig. 9 f and g show the melt pool flows in 3D to the two applied magnetic fields. The TEMHD flows are created and circulating in the two orthogonal planes (i.e., yz and xy planes) when applying magnetic fields with different orientations. It is worth noting that for the B downward case TEMHD flow drags particles towards the front of the melt pool (Fig. 10a) in one half and towards the rear (Fig. 10b) in the other half, as was captured radiographically. However, due to the projection nature of the radiograph, we cannot directly determine which half part of the melt pool the particle is in. But, we can make deductions based on our proposed hypothesis that in the B downward case, in the $\hat{x}$ direction, the TEMHD flow in one half points towards the rear of the melt pool while in the other half, it is directed towards the front of the melt pool, as illustrated in Fig. 9 g Therefore, by observing the horizontal direction of particle movement, we can deduce which half of the melt pool the particle is in. if the particle moves towards the front, it is in the left half, whereas if it moves towards the rear, it is in the right of the melt pool.

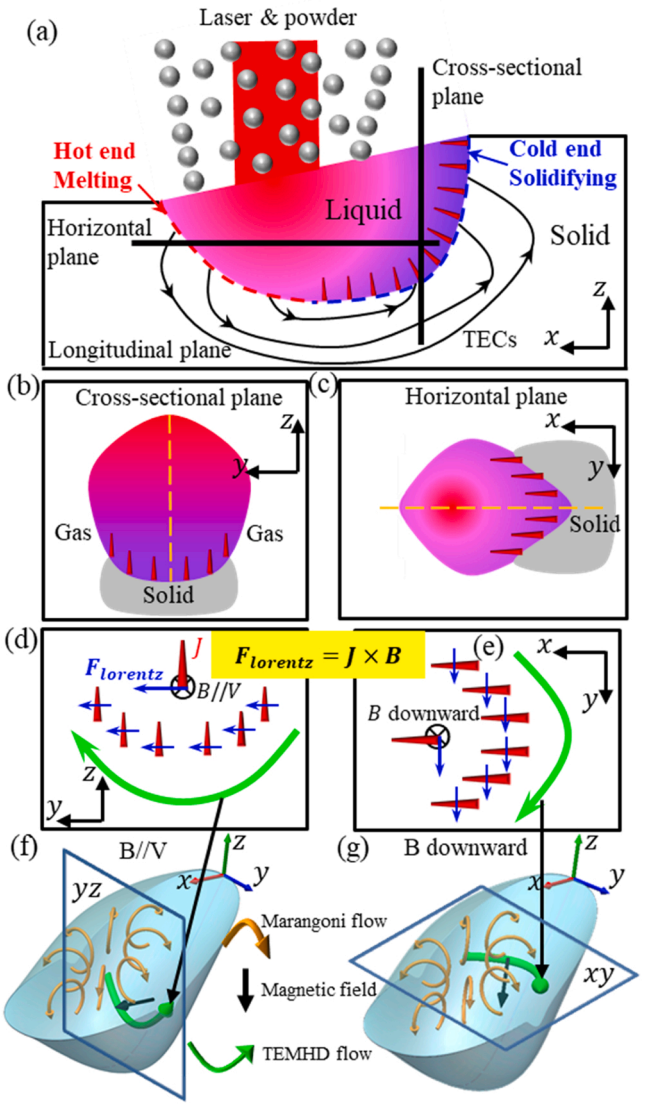

Fig. 9. Schematic of the flows driven by TE Lorentz force. (a) Origin of thermoelectric currents in the melt pool; (b) TECs distribution on the cross-sectional plane; and (c) TECs distribution on the horizontal plane. (d) For the B//V case, the TEMHD flow circulates in the cross-sectional plane; and (e) for the B downward case, TEMHD flow circulates in the horizontal plane. TEMHD flow in a 3D melt pool for: (f) the B//V case (*yz* denotes cross-sectional plane); and (g) the B downward case (*xy* denotes horizontal plane).

Our in situ synchrotron radiography and *ex situ* tomography results strongly support our hypothesis that TEMHD flow is a key force during DED when a magnetic field is applied, strongly impacting the flow in the melt pool and hence final microstructural feature formation. However, these results are not limited to DED, the methodology can be applied to the broader field of laser materials processing, such as laser welding and LPBF where TECs will also exist, with some necessary considerations. Melt pool solid/liquid boundary locations, that witness significant variation of Seebeck coefficient, is the first factor to consider. In DED, solid/liquid boundary forms at the base and back of the melt pool. However, in LPBF and laser welding, there is a solid/liquid boundary surrounding the melt pool (as the two side walls of the melt pool are in contact with the solid), except for the top surface. We speculate that the TECs also exist in the regions close to the two side walls, which could lead to different TEMHD flow patterns when applying a magnetic field. Previous TEMHD flow simulation work [41] in LPBF with conduction mode predicted the horizontal TEMHD flow circulations in the upward magnetic field case and a vertical TEMHD circulation in the B//V case. This prediction matches our proposed TEMHD flow in Fig. 9 f, g which is derived based on DED experimental data. But in the simulation of LPBF, there is also TEMHD flow located in the regions close to the two side walls [41]. This is not reflected in these DED experiments as the tracks are only a single melt pool thick and the side walls are in contact with the non-conducting atmosphere.

Process parameters are the second factor to consider. Faster scanning speeds and smaller laser spot sizes in LPBF produce higher thermal gradients. The thermal gradient in the melt pool front in LPBF is much higher than in the other areas, as a result, we expect $\hat{x}$-direction (laser scan direction) TECs to be dominant. Unlike in DED where the three orthogonal components of TECs are in the close magnitude, resulting in the similar intensity of the three orthogonal magnetic fields required to alter the existing flow, in LPBF under conduction mode the intensity of the magnetic field required for TEMHD control is highly magnetic field orientation dependent. The previous simulation results [41] show that $\hat{x}$-direction TECs are dominant in LPBF, and the TEMHD flow is weak when B//V and significant as B is perpendicular to V given the same magnetic field strength.

Alloy composition design is also critical to best utilise the TEMHD effect. Alloy composition determines material thermophysical properties, for example, a previous study [55] found that copper results in high constitutional supercooling and promotes columnar to equiaxed transition (CET) in an AM-fabricated Ti alloy. Here we would anticipate that silicon, a semiconductor element prone to having a high Seebeck coefficient, is a highly appropriate alloying addition to boost the TEMHD effect, although the influence will vary depending on the full alloy composition and processing conditions. For example, a previous study shows that silicon content can be tailored to increase or decrease the TEMHD effect during the directional solidification of aluminium alloy [30]. Investigating the effect of silicon content on the TEMHD effect is crucial for promoting the TEMHD-AM alloy design. Apart from the composition, the presence of a secondary phase with significantly

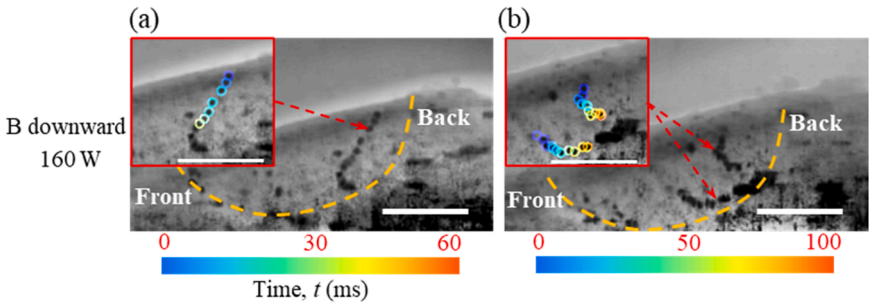

Fig. 10. The trajectories of W particles in the B downward case at 160 W. (a) W particle moves forward to the front of the melt pool; (b) W particle moves backward to the solidification front. The scale bars are 500 μm.

different physical properties compared to the matrix can also impact the TECs distribution. For example, in high γ' nickel superalloys (over 0.6 γ' volume fraction [56]), the γ' phase is intermetallic and likely to have a higher Seebeck coefficient but lower electric conductivity than the matrix, causing a higher thermoelectric field and the increased TEMHD flow in the liquid. Therefore, a high γ' nickel superalloy is deemed as an appropriate alloy for TEMHD control. Further, the TEMHD control might be challenging with ferromagnetic powders as they would be attracted to external magnets. These insights highlight the importance of alloy composition optimisation and material selection for using TEMHD control in AM. In summary, TEMHD flow can circulate in different locations, depending on the orientation of the applied magnetic field. We hypothesise that the application of a constant magnetic field could improve the printability of some alloys, while the application of period magnetic fields could disrupt epitaxial growth. The application of a constant field might be particularly useful when printing high constitutional undercooling alloys, such as Ti-Cu alloy [55]. By applying a magnetic field perpendicular to both the scan and build directions, and based on the distribution of TECs, a TEMHD flow can be produced, circulating on the *xz* plane and sweeping down the solute from the rear melt pool boundary to the bottom. This would increase constitutional undercooling at the bottom and promote the nucleation rate, with the bottom part expected to have more refined equiaxed grains. For the application of a period magnetic field, this could significantly change the flow field for a period of time, altering the thermal gradient and solidification rate at the solid-liquid interface, disrupting the microstructure, potentially altering epitaxial growth.

5. Conclusions

In summary, by combing in situ synchrotron X-ray imaging and *ex situ* tomography characterisation, we revealed the melt pool flow pattern under the influence of TEMHD during DED process, and investigated the role of magnetic field orientation in disrupting the melt pool flow. The major conclusions are drawn below:

1. TEMHD flow is found to circulate in the cross-sectional plane under the B//V condition, however with B downward, TEMHD flow circulates in the horizontal plane.
2. That the key force is thermoelectric magnetohydrodynamics (TEMHD), rather than just magnetic damping as previously hypothesised. In particular, TEMHD-induced flow dominates close to the liquid/solid boundary where solidification microstructures form.
3. TEMHD effect alters melt pool flow, leading to the change in melt pool geometry and the resulting grain structure.

Our findings demonstrate that applying a magnetic field can significantly alter the melt pool flow, opening the way to influence and perhaps control the formation of microstructural features during AM, and also being critical for the development of a reliable numerical model for the magnetic field-assisted AM process.

CRediT authorship contribution statement

Xianqiang Fan: Conceptualization, Formal analysis, Investigation, Writing – original draft. **Tristan G. Fleming:** Investigation, Writing – review & editing. **David T. Rees:** Investigation, Writing – review & editing. **Yuze Huang:** Investigation, Writing – review & editing. **Sebastian Marussi:** Methodology, Writing – review & editing. **Chu Lun Alex Leung:** Methodology, Writing – review & editing. **Robert C. Atwood:** Methodology, Resources, Writing – review & editing. **Andrew Kao:** Conceptualization, Supervision, Writing – review & editing. **Peter D. Lee:** Conceptualization, Project administration, Supervision, Funding acquisition, Writing – review & editing.

Declaration of Competing Interest

The authors declare that they have no known competing financial interests or personal relationships that could have appeared to influence the work reported in this paper.

Data Availability

Data will be made available on request.

Acknowledgements

This research was supported under MAPP: UK-EPSRC Future Manufacturing Hub in Manufacture using Advanced Powder Processes (EP/P006566/1) and a Royal Academy of Engineering Chair in Emerging Technologies (CiET1819/10). The authors acknowledge UK-EPSRC support (grants EP/W031167/1, EP/W032147/1, EP/W037483/1, EP/W006774/1, EP/W003333/1, EP/V061798/1). XF acknowledges the China Scholarship Council. DTR acknowledges a Rolls-Royce plc. and EPSRC-iCASE. All authors are grateful for the use of the facilities provided by Research Complex at Harwell and thank Diamond Light Source for providing the beamtime (MG28804) and staff in beamline JEEP-I12 for the technical assistance. Thanks to Saurabh Shah for the tomography help. The provision of materials from Rolls-Royce plc. is gratefully acknowledged.

Appendix A. Supporting information

Supplementary data associated with this article can be found in the online version at doi:10.1016/j.addma.2023.103587.

References

[1] D. Svetlizky, M. Das, B. Zheng, A.L. Vyatskikh, S. Bose, A. Bandyopadhyay, J. M. Schoenung, E.J. Lavernia, N. Eliaz, Directed energy deposition (DED) additive manufacturing: Physical characteristics, defects, challenges and applications, Mater. Today 49 (2021) 271–295, https://doi.org/10.1016/j.mattod.2021.03.020.
[2] S.M. Thompson, L. Bian, N. Shamsaei, A. Yadollahi, An overview of Direct Laser Deposition for additive manufacturing; Part I: Transport phenomena, modeling and diagnostics, Addit. Manuf. 8 (2015) 36–62, https://doi.org/10.1016/j.addma.2015.07.001.
[3] D. Gu, X. Shi, R. Poprawe, D.L. Bourell, R. Setchi, J. Zhu, Material-structure-performance integrated laser-metal additive manufacturing, Science 80 (372) (2021) 1487, https://doi.org/10.1126/science.abg1487.
[4] N. Eliaz, N. Foucks, D. Geva, S. Oren, N. Shriki, D. Vaknin, D. Fishman, O. Levi, Comparative quality control of titanium alloy Ti-6Al-4V, 17-4 PH stainless steel, and aluminum alloy 4047 either manufactured or repaired by laser engineered net shaping (LENS), Materials 13 (2020) 4171, https://doi.org/10.3390/ma13184171.
[5] S.J. Wolff, H. Wang, B. Gould, N. Parab, Z. Wu, C. Zhao, A. Greco, T. Sun, In situ X-ray imaging of pore formation mechanisms and dynamics in laser powder-blown directed energy deposition additive manufacturing, Int. J. Mach. Tools Manuf. 166 (2021), 103743, https://doi.org/10.1016/j.ijmachtools.2021.103743.
[6] B. Guo, Y. Zhang, Z. Yang, D. Cui, F. He, J. Li, Z. Wang, X. Lin, J. Wang, Cracking mechanism of Hastelloy X superalloy during directed energy deposition additive manufacturing, Addit. Manuf. 55 (2022), 102792, https://doi.org/10.1016/j.addma.2022.102792.
[7] C.J. Todaro, M.A. Easton, D. Qiu, D. Zhang, M.J. Bermingham, E.W. Lui, M. Brandt, D.H. StJohn, M. Qian, Grain structure control during metal 3D printing by high-intensity ultrasound, Nat. Commun. 11 (2020) 1–9, https://doi.org/10.1038/s41467-019-13874-z.
[8] L. Aucott, H. Dong, W. Mirihanage, R. Atwood, A. Kidess, S. Gao, S. Wen, J. Marsden, S. Feng, M. Tong, T. Connolley, M. Drakopoulos, C.R. Kleijn, I. M. Richardson, D.J. Browne, R.H. Mathiesen, H.V. Atkinson, Revealing internal flow behaviour in arc welding and additive manufacturing of metals, Nat. Commun. 9 (2018) 1–7, https://doi.org/10.1038/s41467-018-07900-9.
[9] Q. Guo, C. Zhao, M. Qu, L. Xiong, S.M.H. Hojjatzadeh, L.I. Escano, N.D. Parab, K. Fezzaa, T. Sun, L. Chen, In-situ full-field mapping of melt flow dynamics in laser metal additive manufacturing, Addit. Manuf. 31 (2020), 100939, https://doi.org/10.1016/j.addma.2019.100939.
[10] Q. Guo, M. Qu, L.I. Escano, S.M.H. Hojjatzadeh, Z. Young, K. Fezzaa, L. Chen, Revealing melt flow instabilities in laser powder bed fusion additive manufacturing of aluminum alloy via in-situ high-speed X-ray imaging, Int. J. Mach. Tools Manuf. 175 (2022), 103861, https://doi.org/10.1016/j.ijmachtools.2022.103861.
[11] Y. Yu, L. Wang, J. Zhou, H. Li, Y. Li, W. Yan, F. Lin, Impact of fluid flow on the dendrite growth and the formation of new grains in additive manufacturing, Addit. Manuf. 55 (2022), 102832, https://doi.org/10.1016/j.addma.2022.102832.

[12] S.M.H. Hojjatzadeh, N.D. Parab, W. Yan, Q. Guo, L. Xiong, C. Zhao, M. Qu, L. I. Escano, X. Xiao, K. Fezzaa, W. Everhart, T. Sun, L. Chen, Pore elimination mechanisms during 3D printing of metals, Nat. Commun. 10 (2019) 1–8, https://doi.org/10.1038/s41467-019-10973-9.
[13] Y. Huang, T.G. Fleming, S.J. Clark, S. Marussi, K. Fezzaa, J. Thiyagalingam, C.L. A. Leung, P.D. Lee, Keyhole fluctuation and pore formation mechanisms during laser powder bed fusion additive manufacturing, Nat. Commun. 13 (2022) 1–11, https://doi.org/10.1038/s41467-022-28694-x.
[14] Y. Chen, S.J. Clark, L. Sinclair, C.L.A. Leung, S. Marussi, T. Connolley, R. C. Atwood, G.J. Baxter, M.A. Jones, I. Todd, P.D. Lee, Synchrotron X-ray imaging of directed energy deposition additive manufacturing of titanium alloy Ti-6242, Addit. Manuf. 41 (2021), 101969, https://doi.org/10.1016/j.addma.2021.101969.
[15] Y. Chen, S.J. Clark, D.M. Collins, S. Marussi, S.A. Hunt, D.M. Fenech, T. Connolley, R.C. Atwood, O.V. Magdysyuk, G.J. Baxter, M.A. Jones, C.L.A. Leung, P.D. Lee, Correlative synchrotron X-ray imaging and diffraction of directed energy deposition additive manufacturing, Acta Mater. 209 (2021), 116777, https://doi.org/10.1016/j.actamat.2021.116777.
[16] Y. Chen, S.J. Clark, Y. Huang, L. Sinclair, C. Lun Alex Leung, S. Marussi, T. Connolley, O.V. Magdysyuk, R.C. Atwood, G.J. Baxter, M.A. Jones, I. Todd, P. D. Lee, In situ X-ray quantification of melt pool behaviour during directed energy deposition additive manufacturing of stainless steel, Mater. Lett. 286 (2021), 129205, https://doi.org/10.1016/j.matlet.2020.129205.
[17] Y. Wang, H.L. Tsai, Effects of surface active elements on weld pool fluid flow and weld penetration in gas metal arc welding, Metall. Mater. Trans. B Process. Metall. Mater. Process. Sci. 32 (2001) 501–515, https://doi.org/10.1007/s11663-001-0035-5.
[18] Y. Zhao, H. Zhou, Y. Shi, The study of surface active element on weld pool development in A-TIG welding, Model. Simul. Mater. Sci. Eng. 14 (2006) 331–349, https://doi.org/10.1088/0965-0393/14/3/001.
[19] Z. Gan, G. Yu, X. He, S. Li, Surface-active element transport and its effect on liquid metal flow in laser-assisted additive manufacturing, Int. Commun. Heat. Mass Transf. 86 (2017) 206–214, https://doi.org/10.1016/j.icheatmasstransfer.2017.06.007.
[20] Y.S. Lee, M. Nordin, S.S. Babu, D.F. Farson, Influence of fluid convection on weld pool formation in laser cladding, Weld. J. 93 (2014) 292–300.
[21] C.L.A. Leung, S. Marussi, M. Towrie, R.C. Atwood, P.J. Withers, P.D. Lee, The effect of powder oxidation on defect formation in laser additive manufacturing, Acta Mater. 166 (2019) 294–305, https://doi.org/10.1016/j.actamat.2018.12.027.
[22] C. Iantaffi, C.L.A. Leung, Y. Chen, S. Guan, R.C. Atwood, J. Lertthanasarn, M.-S. Pham, M. Meisnar, T. Rohr, P.D. Lee, Oxidation induced mechanisms during directed energy deposition additive manufactured titanium alloy builds, Addit. Manuf. Lett. 1 (2021), 100022, https://doi.org/10.1016/j.addlet.2021.100022.
[23] P.D. Lee, T. North, A.R. Perrin, Methods of experimental confirmation of a computational model of the fluid flow in gas tungsten arc welding, Model. Control Cast. Weld. Process. IV (1988) 131–140.
[24] C. Zhao, N.D. Parab, X. Li, K. Fezzaa, W. Tan, A.D. Rollett, T. Sun, Critical instability at moving keyhole tip generates porosity in laser melting, Sci. (80-.). 1086 (2020) 1080–1086.
[25] J. Chen, Y. Wei, X. Zhan, Q. Gao, D. Zhang, X. Gao, Influence of magnetic field orientation on molten pool dynamics during magnet-assisted laser butt welding of thick aluminum alloy plates, Opt. Laser Technol. 104 (2018) 148–158, https://doi.org/10.1016/j.optlastec.2018.02.020.
[26] M. Bachmann, V. Avilov, A. Gumenyuk, M. Rethmeier, Numerical assessment and experimental verification of the influence of the Hartmann effect in laser beam welding processes by steady magnetic fields, Int. J. Therm. Sci. 101 (2016) 24–34, https://doi.org/10.1016/j.ijthermalsci.2015.10.030.
[27] J. Paulini, G. Simon, I. Decker, Beam deflection in electron beam welding by thermoelectric eddy currents, J. Phys. D. Appl. Phys. 23 (1990) 486–495, https://doi.org/10.1088/0022-3727/23/5/004.
[28] M. Kern, P. Berger, H. Hügel, Magneto-fluid dynamic control of seam quality in CO_2 laser beam welding, Weld. J. 79 (2000) 72–78.
[29] A. Lange, A. Cramer, E. Beyer, Thermoelectric currents in laser induced melts pools, J. Laser Appl. 21 (2009) 82–87, https://doi.org/10.2351/1.3120213.
[30] B. Cai, A. Kao, E. Boller, O.V. Magdysyuk, R.C. Atwood, N.T. Vo, K. Pericleous, P. D. Lee, Revealing the mechanisms by which magneto-hydrodynamics disrupts solidification microstructures, Acta Mater. 196 (2020) 200–209, https://doi.org/10.1016/j.actamat.2020.06.041.
[31] Y. Fautrelle, J. Wang, G. Salloum-Abou-Jaoude, L. Abou-Khalil, G. Reinhart, X. Li, Z.M. Ren, H. Nguyen-Thi, Thermo-electric-magnetic hydrodynamics in solidification: in situ observations and theory, Jom 70 (2018) 764–771, https://doi.org/10.1007/s11837-018-2777-4.
[32] I. Kaldre, Y. Fautrelle, J. Etay, A. Bojarevics, L. Buligins, Thermoelectric current and magnetic field interaction influence on the structure of directionally solidified Sn-10 wt%Pb alloy, J. Alloy. Compd. 571 (2013) 50–55, https://doi.org/10.1016/j.jallcom.2013.03.211.
[33] X. Li, A. Gagnoud, Z. Ren, Y. Fautrelle, R. Moreau, Investigation of thermoelectric magnetic convection and its effect on solidification structure during directional solidification under a low axial magnetic field, Acta Mater. 57 (2009) 2180–2197, https://doi.org/10.1016/j.actamat.2009.01.016.
[34] X. Li, Y. Fautrelle, A. Gagnoud, D. Du, J. Wang, Z. Ren, H. Nguyen-Thi, N. Mangelinck-Noel, Effect of a weak transverse magnetic field on solidification structure during directional solidification, Acta Mater. 64 (2014) 367–381, https://doi.org/10.1016/j.actamat.2013.10.050.
[35] Z. Shen, B. Zhou, Y. Zhong, T. Zheng, W. Ren, Z. Lei, Z. Ren, Revealing influence mechanism of a transverse static magnetic field on the refinement of primary dendrite spacing during directional solidification, J. Cryst. Growth 517 (2019) 54–58, https://doi.org/10.1016/j.jcrysgro.2019.04.010.
[36] M.A. Jaworski, T.K. Gray, M. Antonelli, J.J. Kim, C.Y. Lau, M.B. Lee, M. J. Neumann, W. Xu, D.N. Ruzic, Thermoelectric magnetohydrodynamic stirring of liquid metals, Phys. Rev. Lett. 104 (2010) 1–4, https://doi.org/10.1103/PhysRevLett.104.094503.
[37] W. Xu, V. Surla, M.A. Jaworski, M. Lee, T. Mui, M.J. Neumann, D.N. Ruzic, Investigation of the heat transfer in TEMHD driven swirling lithium flow, J. Nucl. Mater. 415 (2011) 981–984, https://doi.org/10.1016/j.jnucmat.2010.12.022.
[38] X. Chen, S. Pang, X. Shao, C. Wang, J. Xiao, P. Jiang, Three-dimensional transient thermoelectric currents in deep penetration laser welding of austenite stainless steel, Opt. Lasers Eng. 91 (2017) 196–205, https://doi.org/10.1016/j.optlaseng.2016.12.001.
[39] J. Chen, Y. Wei, X. Zhan, C. Gu, X. Zhao, Thermoelectric currents and thermoelectric-magnetic effects in full-penetration laser beam welding of aluminum alloy with magnetic field support, Int. J. Heat. Mass Transf. 127 (2018) 332–344, https://doi.org/10.1016/j.ijheatmasstransfer.2018.08.004.
[40] X. Chen, M. Luo, R. Hu, R. Li, L. Liang, S. Pang, Thermo-electromagnetic effect on weld microstructure in magnetically assisted laser welding of austenite steel, J. Manuf. Process 41 (2019) 111–118, https://doi.org/10.1016/j.jmapro.2019.03.033.
[41] A. Kao, T. Gan, C. Tonry, I. Krastins, K. Pericleous, Thermoelectric magnetohydrodynamic control of melt pool dynamics and microstructure evolution in additive manufacturing, Philos. Trans. R. Soc. A Math. Phys. Eng. Sci. 378 (2020) 20190249, https://doi.org/10.1098/rsta.2019.0249.
[42] L. Wang, W. Yan, Thermoelectric magnetohydrodynamic model for laser-based metal additive manufacturing, Phys. Rev. Appl. 15 (2021), 064051, https://doi.org/10.1103/physrevapplied.15.064051.
[43] R. Cunningham, C. Zhao, N. Parab, C. Kantzos, J. Pauza, K. Fezzaa, T. Sun, A. D. Rollett, Keyhole threshold and morphology in laser melting revealed by ultrahigh-speed x-ray imaging, Science 80 (363) (2019) 849–852, https://doi.org/10.1126/science.aav4687.
[44] S. Wolff, B. Gould, N. Parab, C. Zhao, A. Greco, T. Sun, Preliminary study on the influence of an external magnetic field on melt pool behavior in laser melting of 4140 steel using in-situ X-ray imaging, J. Micro Nano-Manuf. (2021), 041016, https://doi.org/10.1115/1.4049952.
[45] S.J. Wolff, S. Webster, N.D. Parab, B. Aronson, B. Gould, A. Greco, T. Sun, In-situ observations of directed energy deposition additive manufacturing using high-speed X-ray imaging, Jom 73 (2021) 189–200, https://doi.org/10.1007/s11837-020-04469-x.
[46] S.J. Clark, C.L.A. Leung, Y. Chen, L. Sinclair, S. Marussi, P.D. Lee, Capturing Marangoni flow via synchrotron imaging of selective laser melting, IOP Conf. Ser. Mater. Sci. Eng. 861 (2020), 012010, https://doi.org/10.1088/1757-899X/861/1/012010.
[47] M. Drakopoulos, T. Connolley, C. Reinhard, R. Atwood, O. Magdysyuk, N. Vo, M. Hart, L. Connor, B. Humphreys, G. Howell, S. Davies, T. Hill, G. Wilkin, U. Pedersen, A. Foster, N. De Maio, M. Basham, F. Yuan, K. Wanelik, I12: The Joint Engineering, Environment and Processing (JEEP) beamline at diamond light source, J. Synchrotron Radiat. 22 (2015) 828–838, https://doi.org/10.1107/S1600577515003513.
[48] C.L.A. Leung, S. Marussi, R.C. Atwood, M. Towrie, P.J. Withers, P.D. Lee, In situ X-ray imaging of defect and molten pool dynamics in laser additive manufacturing, Nat. Commun. 9 (2018) 1–9, https://doi.org/10.1038/s41467-018-03734-7.
[49] M. Maggioni, G. Boracchi, A. Foi, K. Egiazarian, Video denoising, deblocking, and enhancement through separable 4-D nonlocal spatiotemporal transforms, IEEE Trans. Image Process 21 (2012) 3952–3966, https://doi.org/10.1109/TIP.2012.2199324.
[50] J.Y. Tinevez, N. Perry, J. Schindelin, G.M. Hoopes, G.D. Reynolds, E. Laplantine, S. Y. Bednarek, S.L. Shorte, K.W. Eliceiri, TrackMate: An open and extensible platform for single-particle tracking, Methods 115 (2017) 80–90, https://doi.org/10.1016/j.ymeth.2016.09.016.
[51] M. Bachmann, V. Avilov, A. Gumenyuk, M. Rethmeier, About the influence of a steady magnetic field on weld pool dynamics in partial penetration high power laser beam welding of thick aluminium parts, Int. J. Heat. Mass Transf. 60 (2013) 309–321, https://doi.org/10.1016/j.ijheatmasstransfer.2013.01.015.
[52] L. Wang, J. Yao, Y. Hu, S. Song, Suppression effect of a steady magnetic field on molten pool during laser remelting, Appl. Surf. Sci. 351 (2015) 794–802, https://doi.org/10.1016/j.apsusc.2015.05.179.
[53] L. Cao, Q. Zhou, H. Liu, J. Li, S. Wang, Mechanism investigation of the influence of the magnetic field on the molten pool behavior during laser welding of aluminum alloy, Int. J. Heat. Mass Transf. 162 (2020), 120390, https://doi.org/10.1016/j.ijheatmasstransfer.2020.120390.
[54] J. Chen, Y. Wei, X. Zhan, Y. Li, W. Ou, T. Zhang, Melt flow and thermal transfer during magnetically supported laser beam welding of thick aluminum alloy plates, J. Mater. Process. Technol. 254 (2018) 325–337, https://doi.org/10.1016/j.jmatprotec.2017.11.046.
[55] D. Zhang, D. Qiu, M.A. Gibson, Y. Zheng, H.L. Fraser, D.H. StJohn, M.A. Easton, Additive manufacturing of ultrafine-grained high-strength titanium alloys, Nature 576 (2019) 91–95, https://doi.org/10.1038/s41586-019-1783-1.
[56] S.P. Murray, K.M. Pusch, A.T. Polonsky, C.J. Torbet, G.G.E. Seward, N. Zhou, S.A. J. Forsik, P. Nandwana, M.M. Kirka, R.R. Dehoff, W.E. Slye, T.M. Pollock, A defect-resistant Co–Ni superalloy for 3D printing, Nat. Commun. 11 (2020) 1–11, https://doi.org/10.1038/s41467-020-18775-0.